Supplementary Information:

Ribosomal tRNA release decoded via multiscale simulations at biological timescales

Jigneshkumar Dahyabhai Prajapati,[1] Karissa Y. Sanbonmatsu[1,2]*

[1]Theoretical Biology and Biophysics, Los Alamos National Laboratory, Los Alamos, New Mexico 87545, United States

[2]New Mexico Consortium, Los Alamos, New Mexico 87544, United States

To whom correspondence may be addressed. Email: kys@lanl.gov

S1. Mapping Simulated Events to Biological Timescales: Kinetic Rescaling of Rigid-Body Simulations

Dissociation of deacylated tRNA from the ribosomal E site occurs on a biological timescale of hundreds of milliseconds to seconds, as shown by single-molecule FRET experiments.[1,2] Simulating such events in atomistic detail with explicit solvent remains infeasible with current computing resources: a direct simulation would require either ~1000 years on a single exascale supercomputer, or ~1 year using 1000 exascale.[3] To address this bottleneck, we developed MUON (MUlti-scale multi-bOdy accelerated sampliNg), a coarse-grained, constrained dynamics framework that accelerates sampling of rare dissociation events. MUON leverages the observation that many domains and subdomains of macromolecular complexes behave as near-rigid bodies. By omitting internal flexibility within these domains, we reduce the system's configurational entropy, thus lowering the number of microstates and enhancing transition rates across free energy barriers. This entropy reduction, however, leads to artificially elevated free energy barriers in the simulations, as internal conformational degrees of freedom that would normally facilitate barrier crossing are excluded.

To counteract this and promote transitions, we apply elevated simulation temperatures (T = 10,000–20,000 K), compensating for the absence of explicit solvent and frictional damping. Despite these simplifications, the rigid-body model retains steric exclusion, electrostatic interactions, and topological constraints critical for accurate modeling of tRNA–ribosome interactions. The combination of rigid-body dynamics and high temperature thus enables efficient sampling while maintaining biophysically relevant pathways, provided appropriate scaling corrections are applied during interpretation. Importantly, the simulation timestep (*e.g.*, 2 or 10 fs) remains formally unchanged. However, the effective kinetic timescale, *i.e.,* the simulated duration associated with rare events, is compressed by several orders of magnitude due to entropy reduction, absence of solvent drag and thermal acceleration. Thus, while absolute rates and barriers are perturbed, relative comparisons (*e.g.,* between intermediates) remain physically interpretable. We emphasize that this approach allows for qualitative exploration of mechanism rather than precise quantitative reproduction of time and energy scales.

To relate simulated event rates to experimental timescales, we calibrate the simulation clock using a kinetic rescaling approach: observed event frequencies (*e.g.,* tRNA release events per unit simulation time) are matched to experimental rates. This method is conceptually similar to frameworks used in accelerated MD, hyperdynamics, and coarse-grained modeling. It enables approximate mapping of simulation time to biological time, allowing inference of effective rate constants and barrier heights within a biophysically relevant context. Accordingly, we interpret the simulation time in arbitrary units, calibrated by mapping observed event rates (*e.g.,* number of dissociation events per simulated time) onto known experimental timescales. This rescaling approach is analogous to that used in accelerated MD, hyperdynamics, and coarse-grained modeling, and allows us to estimate effective rate constants and free energy barriers. While quantitative uncertainties remain due to entropy reduction and elevated temperature, the simulation framework enables mechanistic dissection of rare events otherwise inaccessible to all-atom MD.

In the MUON simulations, dissociation of the tRNA occurred in a few million time steps at an elevated temperature of 20,000 K. To relate these MUON timescales to biological timescales at room temperature (298 K), a scaling procedure was employed. The experimental dissociation time (τ_e) for tRNA release from the ribosome at low ionic strength is approximately 2 s at 298 K. Assuming that most dissociation events occur after the ribosome reaches the classical POST state, this experimental timescale (τ_e = 2 s) was taken to represent tRNA release from the POST state.[1,2] From MUON simulations, the corresponding dissociation time (τ_m) for tRNA release from the POST state was estimated to be approximately 410,000 fs at 20,000 K. Based on this, one MUON timestep (Δt_m) can be transformed to its biological equivalent (Δt_r) using the relation:

$$\Delta t_m = \Delta t_r \frac{\tau_m}{\tau_e} \qquad (1)$$

This yields a conversion factor of 1 fs (MUON) = 4.88 μs (real time at 298 K).

Using this factor, all MUON trajectories for the INT2**,** INT3, and POST states (Fig. S1A) were rescaled to biological timescales, as shown in Fig. 3C of the main text. It is important to emphasize that this timescale transformation was performed solely to provide a more intuitive comparison of dissociation times across the three ribosomal states, rather than to yield quantitative kinetic parameters comparable to experimental measurements. Therefore, this conversion factor should be used with care in future studies to derive kinetic quantities.

S2. Rescaling potential of mean force profiles from MUON

We next estimated the energy barrier associated with tRNA dissociation from the E-site pocket of the ribosome. The experimental dissociation time (τ_e) at low ionic strength is approximately 2 s at T_e of 298 K, where dissociation is presumed to occur mainly from the POST state.[1,2] From MUON simulations, using the corresponding dissociation time (τ_m) for the POST state at temperature (T_m) of 20,000 K and the two-point Arrhenius relation, the connection between these timescales can be expressed as:

$$\tau_m = \tau_e \exp\left[\frac{\Delta G^{\dagger}}{R}\left(\frac{1}{T_m} - \frac{1}{T_e}\right)\right], \tag{2}$$

Which can be rearranged as:

$$\Delta G^{\dagger} = \frac{R\ \ln\left(\frac{\tau_m}{\tau_e}\right)}{\left(\frac{1}{T_m} - \frac{1}{T_e}\right)}, \tag{3}$$

where R is gas constant. Substituting the experimental and MUON timescales into this equation yields an energy barrier ($\Delta G^{\dagger}$) of approximately 13.4 kcal/mol. From MUON simulations, the uncorrected energy barrier (ΔG^{m}) for tRNA dissociation from the POST state was found to be 162.5 kcal/mol (Fig. S1B), which over estimates the barrier due interaction strengths and exclusion of configurational entropy and solvent effects, as discussed above. This discrepancy is expected, given artifacts inherent to the rigid-body approximation, simplified non-bonded interactions, and the omission of explicit ions and solvent effects. Accordingly, a correction factor was defined as:

$$C = \frac{\Delta G^{\dagger}}{\Delta G^{m}} \approx 0.08246.$$

The corrected potential of mean force profile (PMF), $F_c(d)$, shown in Fig. 3D of the main text, was thus obtained from the unscaled MUON profile (PMF*), ($F_m(d)$, using:

$$F_c(d) = F_m(d)\, C. \tag{4}$$

The same correction factor was applied to adjust the one-dimensional PMFs from the INT2 and INT3 states, as well as the two-dimensional PMF surfaces across all states. As in the timescale transformation, this PMF rescaling was performed to facilitate an intuitive comparison of the three ribosome states from a biological perspective, not to derive quantitative thermodynamic value.

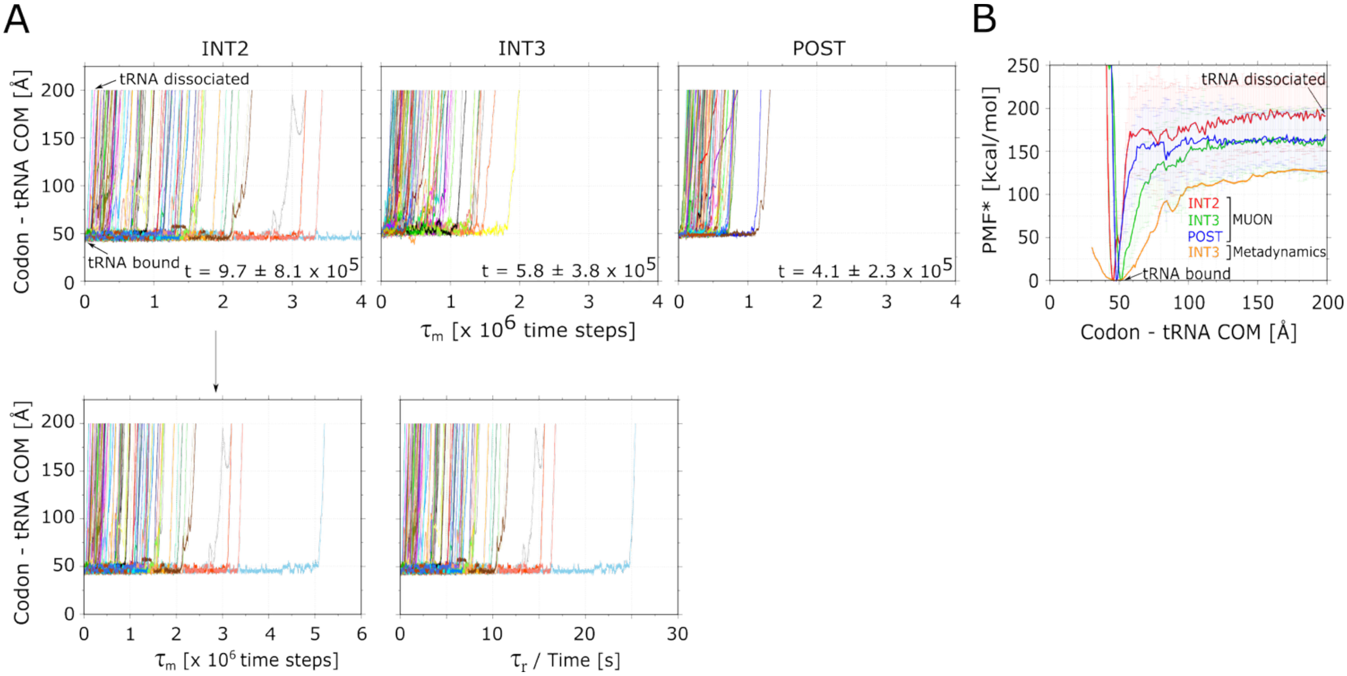

Figure S1: (A) The upper three panels display MUON-derived trajectories of tRNA dissociation from the E-site across the three ribosomal states, shown on the unscaled timescales (τ_m) directly obtained from simulations. The corresponding scaled timescales (τ_r), converted to biological units, are presented in Fig. 3C of the main text. The lower panels highlight one of the longest incomplete dissociation trajectories from the INT2 state (cyan); the left panel shows the unscaled version, and the right panel shows the scaled version. (B) The unscaled potential of mean force profiles (PMF*) are shown as a function of the codon–tRNA center-of-mass (COM) coordinate for all three ribosomal states, calculated from MUON trajectories. Note PMF* is artificially high as MUON over estimates the barriers due interaction strengths and exclusion of configurational entropy and solvent effects, as discussed above. The scaled PMF profiles are presented in Fig. 3D of the main text. For comparison, the PMF profile for the INT3 state obtained from all-atom explicit-solvent metadynamics simulations is also included. While the energy barriers observed in metadynamics are also overestimated due to limited sampling and suboptimal collective variables, the explicit-solvent simulations nonetheless serve as an independent cross-check, supporting the qualitative features observed in MUON trajectories.

S3. Estimation of potential of mean force estimation in metadynamics simulations

In the well-tempered metadynamics framework[4,5] utilized in this study, a history-dependent bias potential $V(\boldsymbol{r}, t)$, representing the cumulative sum of Gaussian hills deposited up to time t, is added during the simulation along predefined set of M collective variables (CVs) $\boldsymbol{r}$. The bias potential is expressed as:

$$V(\boldsymbol{r}, t_N) = \sum_{i=0}^{N} h \exp\left(-\frac{V(\boldsymbol{r}(t_i), t_{i-1})}{k_B \Delta T}\right) \exp\left(-\sum_{j=1}^{M} \frac{\left(\boldsymbol{r}_j - \boldsymbol{r}_j(t_i)\right)^2}{2\delta \boldsymbol{r}_j^2}\right), \tag{5}$$

where $\delta\boldsymbol{r} = (\delta\boldsymbol{r}_1, \dots, \delta\boldsymbol{r}_M)$ denotes the Gaussian widths, $\boldsymbol{r}(t_i) = \left(\boldsymbol{r}_1(t_i), \dots, \boldsymbol{r}_M(t_i)\right)$ are previously visited points in the CV space at the time t_i, and h is the initial Gaussian height. To achieve convergence of the bias potential within the well-tempered scheme, the Gaussian height is progressively reduced by the scaling factor $exp\left(-\frac{V(\boldsymbol{r}(t_i), t_{i-1})}{k_B \Delta T}\right)$. Here, k_B is the Boltzmann constant, ΔT is tuning temperature that limits sampling of the CV to the energy barriers of approximately $k_B(T + \Delta T)$, where T is the system temperature. In addition to the well-tempered formulation, we employed the multiple-walker metadynamics technique, which allows several interacting replicas to run in parallel, thereby accelerating the buildup of the shared bias potential[6].

After the simulations, the one-dimensional (1D) potential of mean force (PMF) or free energy surface ($F(\boldsymbol{r})$) was reconstructed using the Tiwary–Parrinello reweighting scheme[7]:

$$F(\boldsymbol{r}) = -\frac{1}{\beta}\ log\ \frac{\sum_t\ \delta(\boldsymbol{r}(t) - \boldsymbol{r})\ e^{\beta\left(V(\boldsymbol{r},t) - c(t)\right)}}{\sum_t\ e^{\beta\left(V(\boldsymbol{r},t) - c(t)\right)}}, \tag{6}$$

where $\beta = 1/k_B T$, δ is the Dirac delta function, and $c(t)$ is time-dependent offset defined as:

$$c(t) = \frac{1}{\beta}\log\frac{\int dr\ e^{-\beta F(\boldsymbol{r})}}{\int dr\ e^{-\beta\left(F(\boldsymbol{r}) + V(\boldsymbol{r},t)\right)}}, \tag{7}$$

The associated uncertainties were estimated through standard error propagation analysis. For the two-dimensional (2D) PMF landscapes, the same reweighting and reconstruction procedure was applied.

S4. Validation of metadynamics simulations

Collective variable (CV)–based enhanced sampling techniques such as metadynamics typically limit the number of CVs that can be biased to a maximum of two or three. Using multiple CVs often complicates convergence, even for relatively simple systems.[8] Given the enormous size and complexity of the ribosome, we chose to bias a single CV: the distance between the mRNA codon and the center-of-mass of the entire E-site tRNA. From the initial set of 20 walkers, we observed one complete and one partial dissociation of tRNA within 350 ns (Fig. S2A). This limited sampling likely contributed to the lack of full convergence in the potential of mean force (PMF) landscape, particularly in the bulk region. To address this issue, we introduced an additional 20 walkers initialized in the bulk region, using configurations taken from one of the dissociating trajectories. As shown in Fig. S2B, no change in free-energy values was observed for the CV region corresponding to the tRNA-bound state (< 100 Å) during the final 1 μs of simulation. Although minor fluctuations persisted in the bulk region (> 100 Å), the extremely slow rate of change over the last microsecond indicated that further sampling was unnecessary. We do not expect any large-scale deviations beyond this timescale, as the Gaussian hill heights were reduced by two orders of magnitude from their initial values.

The final one-dimensional PMF landscape (Fig. S1B) revealed energy values in the hundreds of kcal/mol range, with the energy barrier between the bound and unbound states approximating 125 kcal/mol. Experimentally, the expected energy barrier is around 18 kcal/mol[2]. Theoretically, for a dissociation constant in the femtomolar range, the estimated binding free energy is about −20.5 kcal/mol $(\Delta G \approx kT\, ln(k_d) \approx 0.592 \times ln\,(10^{-15}) \approx -20.5\, kcal/mol)$. Because such strong binding affinities are rare, any free-energy profile exhibiting a barrier greater than ≈ 20.5 kcal/mol should be regarded as an overestimation. However, numerous theoretical studies report energy barriers ranging from 30 to 70 kcal/mol, and occasionally even hundreds of kcal/mol,[9–17] and some experimental studies also depict the same.[18–20] This discrepancy likely arises because free-energy landscapes are projected along a limited set of CVs, which may not align with the true reaction coordinate. Other factors include neglect of orthogonal degrees of freedom (DOFs), finite simulation timescales, and inaccuracies inherent to current force fields.[21–24] These limitations underscore that the current simulation framework, while valuable, remains insufficient to achieve fully quantitative free-energy estimates for systems of this complexity. While the energy barriers observed in metadynamics may be overestimated due to limited sampling and suboptimal collective variables, the explicit-solvent simulations nonetheless serve as an independent cross-check, supporting the qualitative features observed in MUON trajectories.

Despite these limitations, substantial evidence suggests that the obtained PMF landscape is qualitatively accurate within the applied framework. Specifically, the region corresponding to the tRNA-bound state (~ 50 Å) exhibited complete convergence (Fig. S2B), which extended reliably up to ≈ 100 Å. In the bulk region (150–200 Å), where the tRNA is fully dissociated, the neglect of certain DOFs or limitations of force fields should have minimal influence, implying that the energy values in this regime are also well converged.

To further validate the metadynamics results, we confirmed that the simulations successfully captured the metastable intermediates along the PMF landscape. As shown in Figs. S2C and S2D, both the Z-site conformation of tRNA observed in *Oryctolagus cuniculus* ribosomes and the E^{out} conformation found in *Thermus thermophilus* ribosomes were reproduced during the metadynamics simulations of the *E. coli* ribosome in the INT3 state. Notably, the MUON model identified only the Z-site conformation but not the E^{out} state. This agreement between simulated and experimentally observed metastable conformations strongly supports the reliability of the metadynamics results, even though the absolute energy scales may be less accurate.

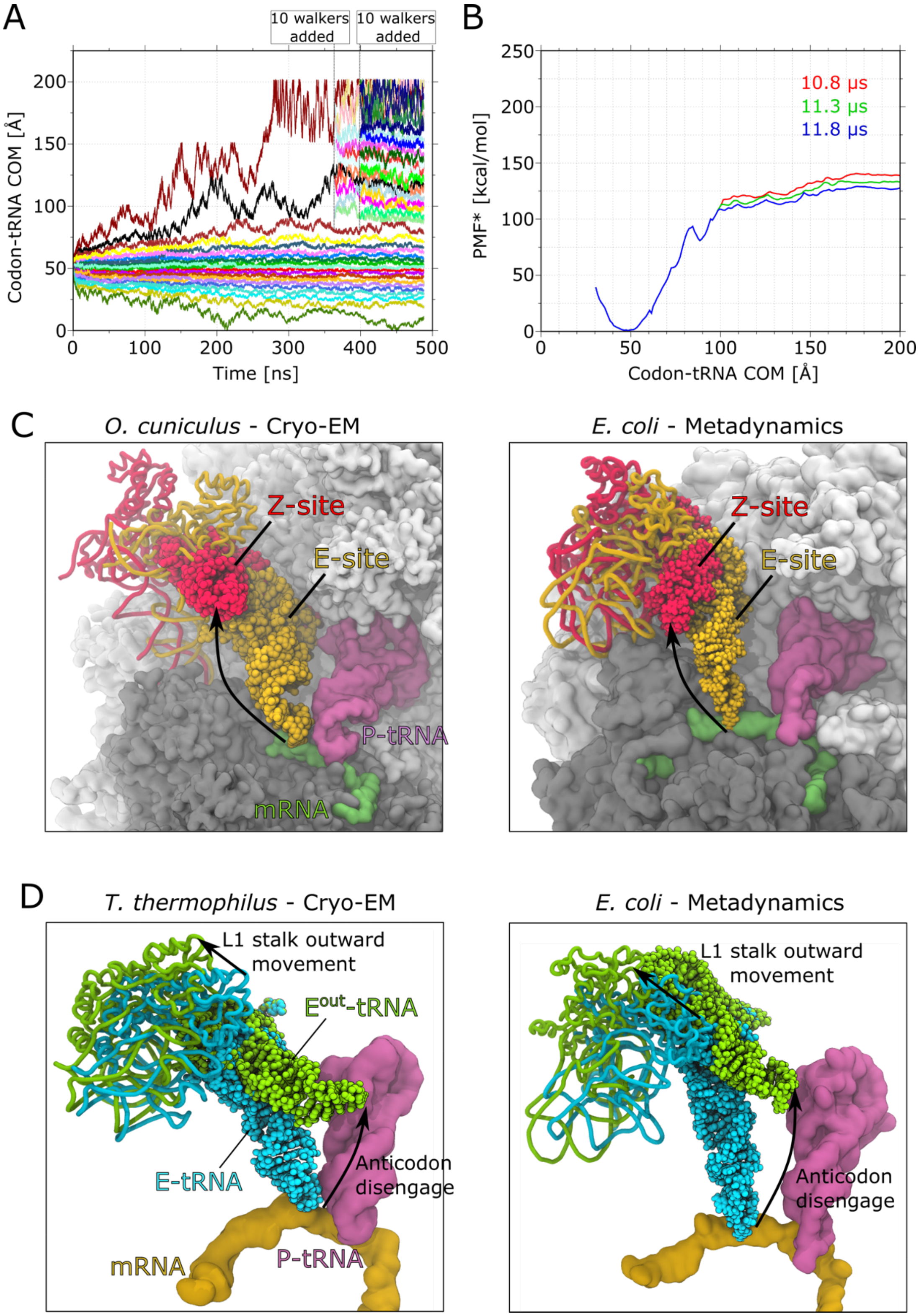

Figure S2: (A) Time evolution of the collective variable (CV) codon–tRNA across all walkers during metadynamics simulations. The first 20 walkers and an additional 20 walkers introduced at a later stage are shown. (B) Potential of mean force (PMF*) profiles as a function of the codon–tRNA CV at different simulation intervals. Slow variations in the free energy across the CV space indicate a high degree of convergence. (C) Left: Comparison of tRNA conformations in the rabbit (*Oryctolagus cuniculus*) ribosome, showing the E-site in the POST state (PDB: 6GZ5,[25] yellow) and the downstream Z-site (PDB: 6MTB,[26] red), both resolved by cryo-EM. Right: A Z-site-like conformation reproduced in metadynamics simulations of the INT3. (D) Left: Comparison of tRNA conformations in the *Thermus thermophilus* ribosome, showing the E^{in} state (PDB: 5UQ7, cyan) with intact codon–anticodon interactions and the E^{out} state (PDB: 5UQ8, green) with anticodon loop displacement.[27] Right: An E^{out}-like conformation reproduced in our metadynamics simulations of the INT3 state.

S5. Rigid body definitions for *E. coli* ribosome in MUON model

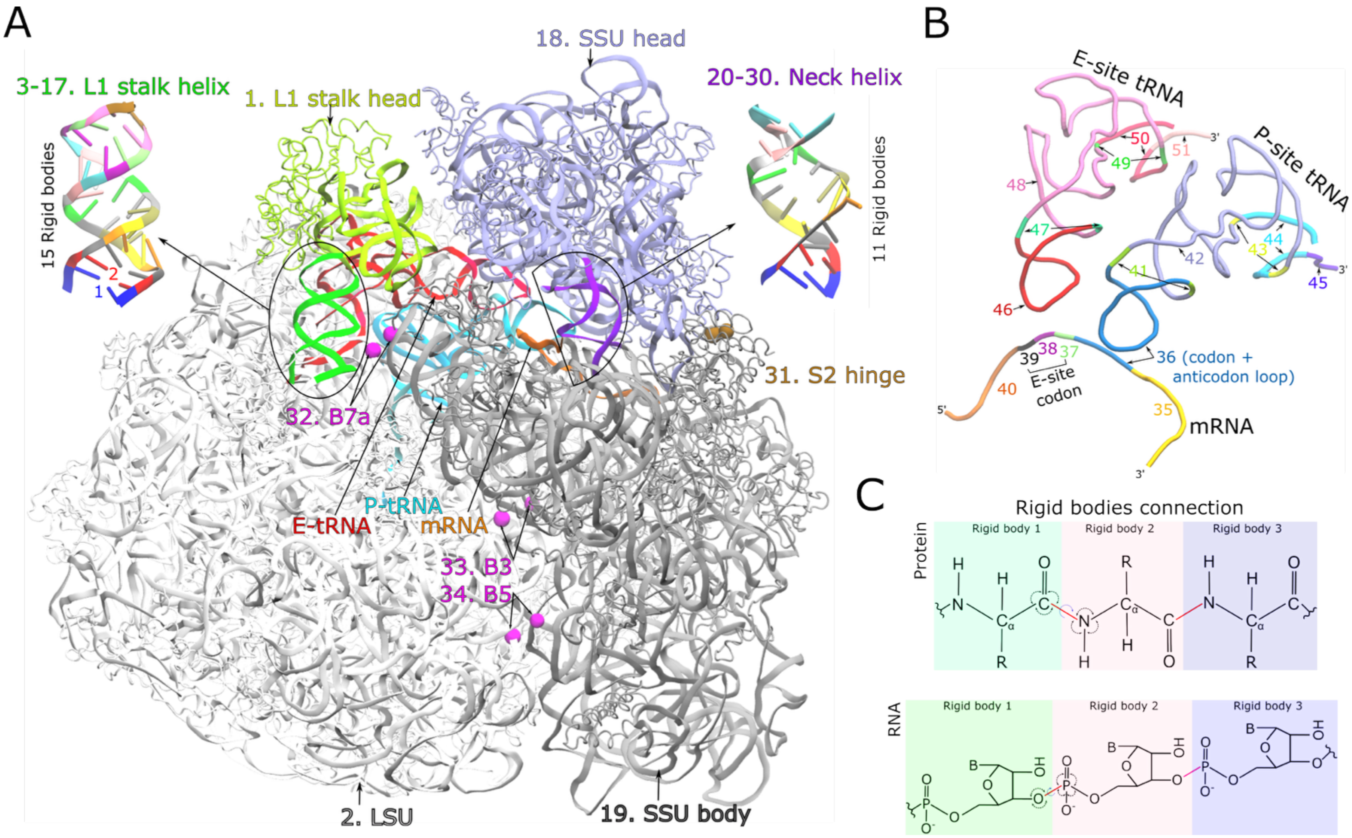

Figure S3: Definitions of rigid bodies in the MUON model for the *E. coli* ribosome. (A) Cartoon representation of the ribosome, with distinct colors and numeric labels denoting various rigid bodies, excluding mRNA, tRNAs, L1 stalk helix, and neck helix. For the L1 stalk and neck helices, each base pair is treated as an individual rigid body, highlighted in the side panels. Inter-subunit bridges (B3, B5, B7a) and the S2 hinge are represented as spheres, each comprising two distant residues forming a rigid body. (B) Cartoon depiction of mRNA and tRNAs, with color coding and numerical labels indicating rigid bodies. E-site tRNA is partitioned into three major bodies (46, 48, 50) and two smaller bodies (47, 49) to allow flexibility. The three residues at the 3′ end of each tRNA are treated as separate rigid bodies for additional flexibility. Codon residues at the P-site, along with the anticodon loop of the P-site tRNA, are combined into a single body to limit excessive displacement. (C) Schematic of connections between rigid bodies in protein and RNA, with peptide and phosphodiester linkages indicated by red bonds.

Required angles and dihedrals for defining these junctions are specified. A full list of residues or segments assigned to each rigid body is provided in Table S1.

Table S1: Rigid body definitions for all bacterial ribosome systems used in the MUON model. Each rigid body is assigned an identification number, along with the corresponding residues and/or molecular components. These IDs are used to annotate atoms within the respective rigid bodies in the LAMMPS input data file.

Rigid body name	Rigid body ID	Residues/Segment name
L1 stalk head	1	L1 protein, 23S (A2108 to U2181)
LSU	2	23S (G1 to U2092, U2197 to U2903), 5S, EF-G, L2, L3, L4, L5, L6, L7, L9, L10, L11, L13, L14, L15, L16, L17, L18, L19, L20, L21, L22, L23, L24, L25, L27, L28, L29, L30, L32, L33, L34, L35, L36
L1 stalk helix	3	G2093•C2196
	4	A2094•U2195
	5	A2095•U2194
	6	C2096•G2193
	7	A2097•U2192
	8	U2098•A2191
	9	U2099•G2190
	10	G2100•U2189
	11	A2101•U2188
	12	G2102•U2187
	13	C2103•G2186
	14	C2104•U2185
	15	U2105•A2184
	16	U2106•A2183
	17	G2107•U2182
SSU head	18	16S (C934 to C1383), S2 protein (K104 to D152), S3, S7, S9, S10, S13, S14, S19
SSU body	19	16S (A2 to G922, C1395 to A1534), S2 protein (M1 to ASN102 and G154 to S225), S4, S5, S6, S8, S11, S12, S15, S16, S17, S18, S20, S21
Neck Helix	20	A923•U1393
	21	C924•G1392
	22	G925•U1391
	23	G926
	24	G927•U1390
	25	G928•C1389

	26	G929•C1388
	27	C930•G1387
	28	C931•G1386
	29	C932•G1385
	30	G933•C1384
S2 hinge	31	W103 and M153
B7a	32	A702•A1848
B3	33	A1483•G1959
B5	34	A1428•G1703
mRNA	35	G1 to A6
	37	G10
	38	U11
	39	U12
	40	U13 to A19
mRNA + P-tRNA	36	Codon (A7 to U9), Anticodon (G29 to C41)
P-tRNA	41	G28•C42
	42	A7 to G27, C43 to C67
	43	G6•C68
	44	G1 to G5, G69 to A73
	45	C74 to A76
E-tRNA	46	U30 to A42
	47	A29•U43
	48	G7 to C28, G44 to G68
	49	C6•U69
	50	G1 to A5, A70 to A74
	51	C75 to A77

S6. Supporting figures

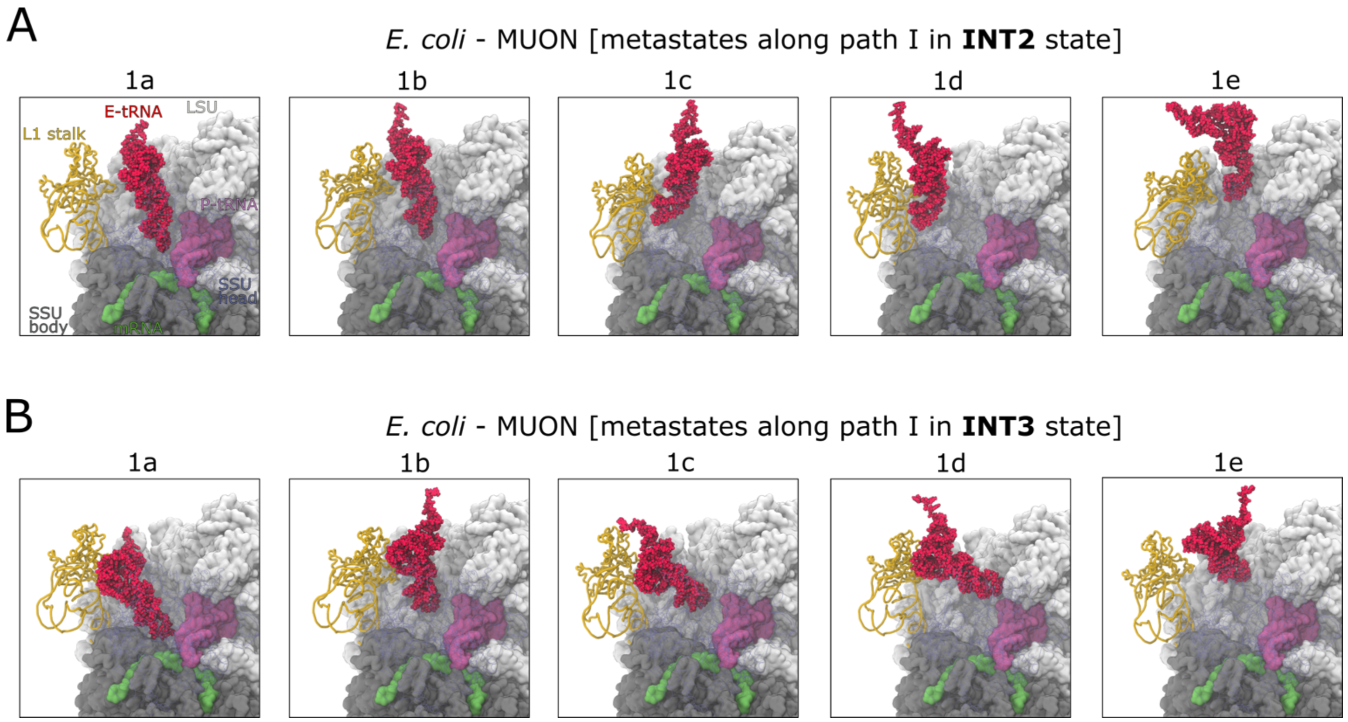

Figure S4: Metastable states along tRNA dissociation pathway I in the (A) INT2 and (B) INT3 states. Representative conformations of tRNA within the E-site cavity are shown for each of the five metastable states: 1a, 1b, 1c, 1d, and 1e.

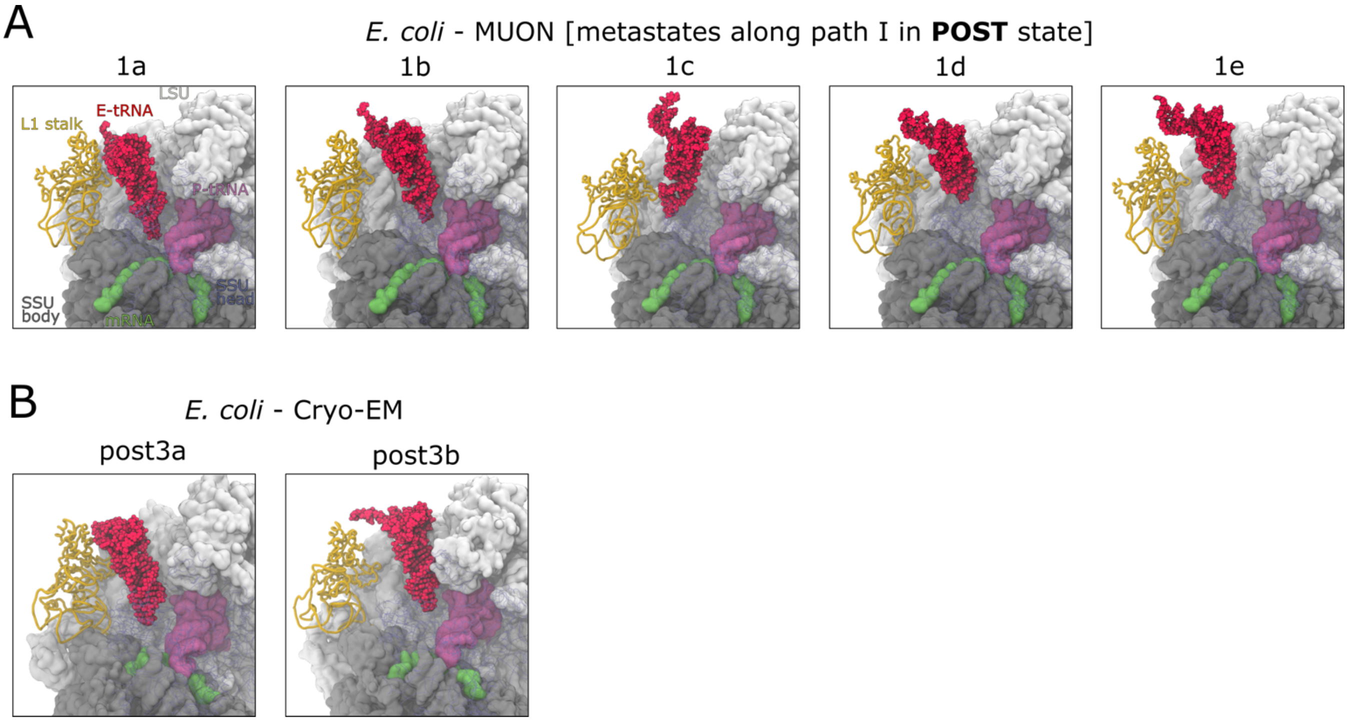

Figure S5: (A) Metastable states along tRNA dissociation pathway I in the POST state. Representative tRNA conformations within the E-site cavity are shown for the five metastable states: 1a, 1b, 1c, 1d, and 1e. (B) Cryo-EM structures of tRNA in the post3a (PDB: 4V78[28]) and post3b (PDB: 4V79[28]) states, which resemble the tRNA conformations in states 1a and 1b, respectively, from panel (A).

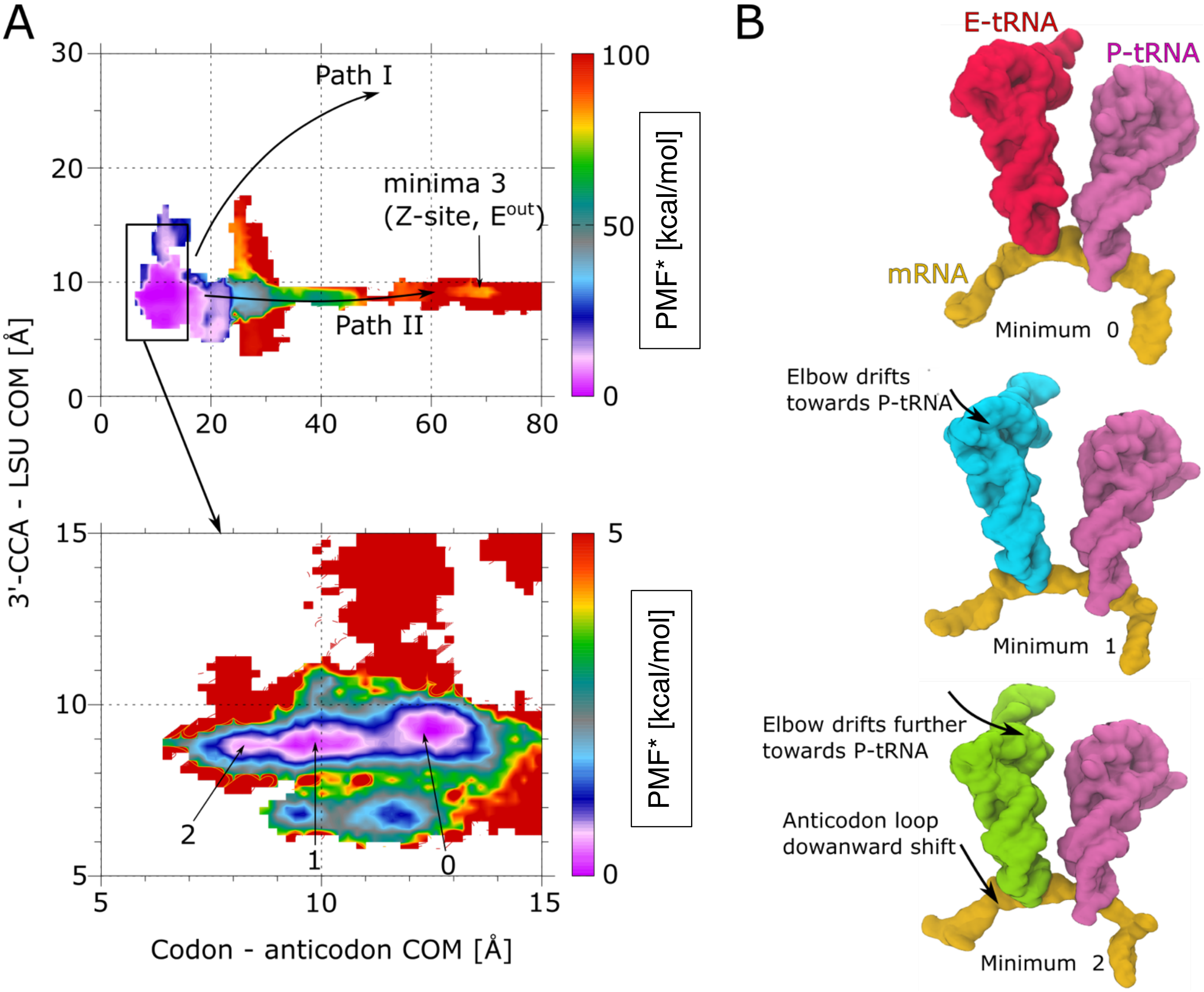

Figure S6: (A) Two-dimensional potential of mean force (PMF*) profile constructed using two collective variables: (i) (i) the distance between the codon and anticodon at the E-site, and (ii) the distance between the 3′-CCA tail and LSU residues C2394, C2395, and G2421, derived from metadynamics simulations. Two dissociation pathways are indicated (I and II), corresponding to whether the anticodon stem loop or the 3′-CCA tail disengages first; in this case, tRNA follows only path II. The lower panel provides a magnified view of the bound-state region. Several metastable states (0–3) are identified, with minimum 3 corresponding to conformations resembling both the Z-site and E^{out} states. (B) Representative conformations of tRNA in three states: the initial bound conformation (state 0) and the subsequent intermediate states (1 and 2), with key motions of the E-site tRNA highlighted.

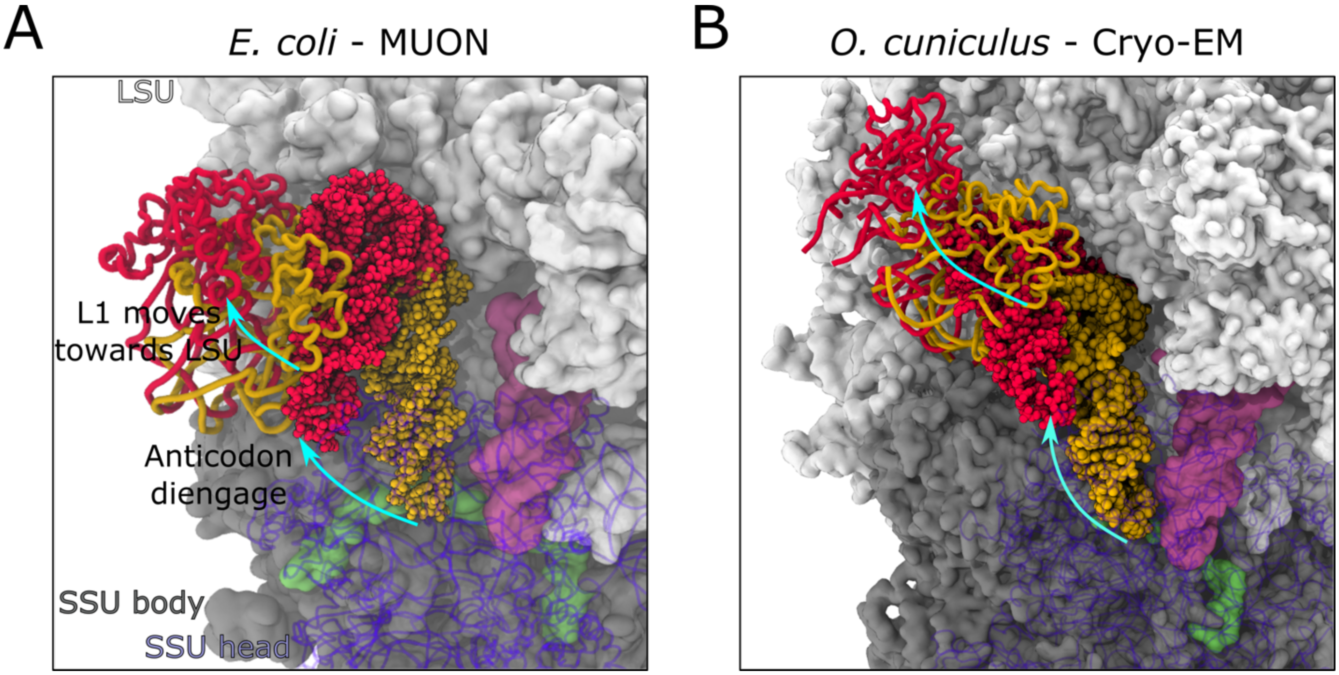

Figure S7: Z-site conformation of tRNA. (A) Comparison of two tRNA conformations in the *E. coli* ribosome: one in the INT3 state (yellow) and the other in the Z-site (red), the latter identified from MUON simulations of INT3. (B) Comparison of tRNA conformations in the *Oryctolagus cuniculus* (rabbit) ribosome: one at the E-site of the POST state (PDB: 6GZ5,[25] yellow) and another *at* the Z-site (PDB: 6MTB,[26] red), located downstream of the POST state, both resolved by cryo-EM. In both panels, the motions of the L1 stalk and the tRNA anticodon stem loop are indicated with arrows. Snapshots correspond to those shown in Figures 4B and 4C of the main text but are presented from a different viewing angle.

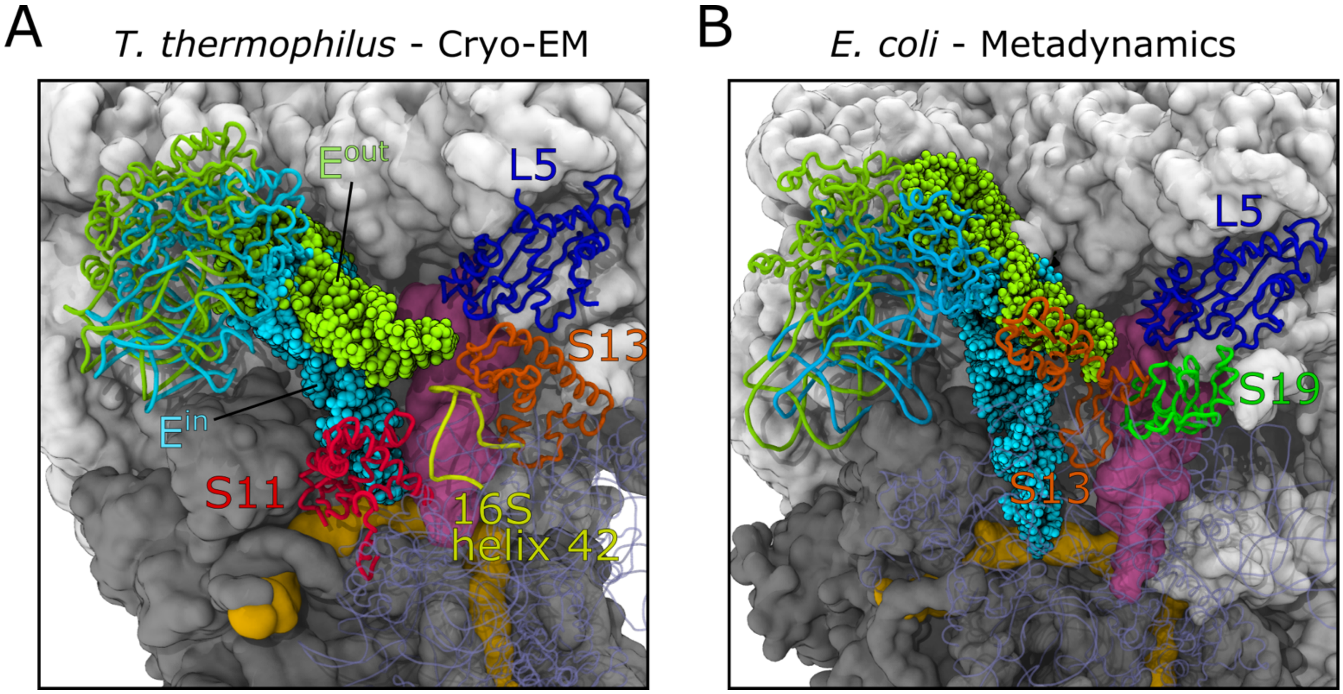

Figure S8: Ribosomal proteins located near the tRNA in the E^{out} conformation. (A) Comparison of tRNA conformations in two cryo-EM–resolved structural states of the *Thermus thermophilus* ribosome: the E^{in} state (PDB: 5UQ7), representing a typical POST state with preserved codon–anticodon interactions (cyan), and the E^{out} state (PDB: 5UQ8), characterized by anticodon loop displacement (green).[27] Ribosomal proteins L5, S11, S13, and helix 42 of the 16S rRNA, located in proximity to the tRNA in the E^{out} conformation, are highlighted. (B) Comparison of the initial tRNA conformation in the INT3 state of the *E. coli* ribosome with the E^{out}-like conformation observed in our metadynamics simulations. Ribosomal proteins L5, S13, and S19, positioned near the E^{out}-like tRNA, are highlighted. The observed differences in ribosomal proteins surrounding the E^{out} conformation of tRNA in the two ribosomes arise from variations in the orientation of the small subunit (SSU) head.

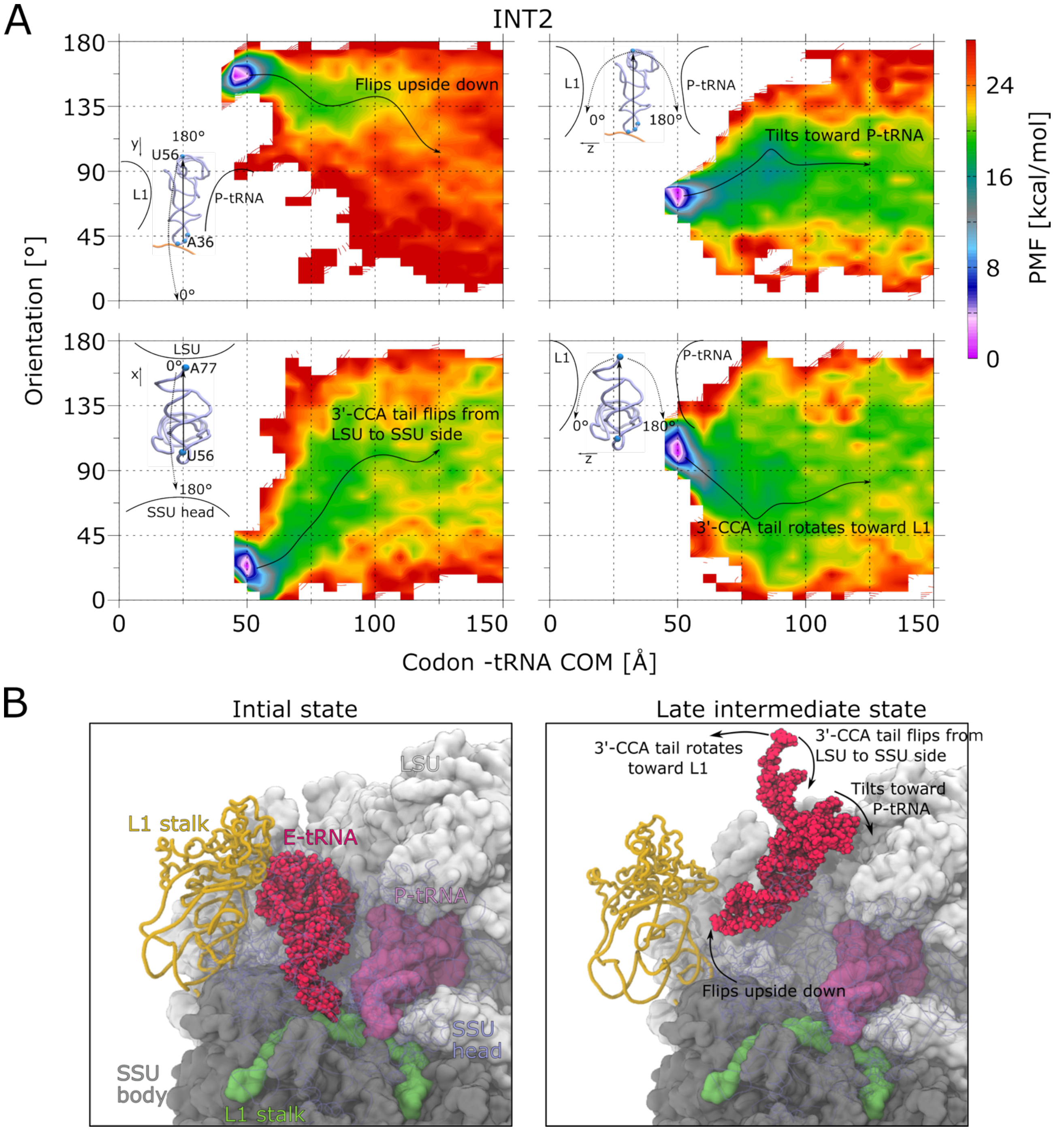

Figure S8: Reorientation of tRNA along the dissociation pathway in the INT2 state. (A) Potential of mean force (PMF) landscapes plotted as a function of codon–tRNA distance and four distinct angular coordinates, derived from MUON trajectories. Top left: Angle between the y-axis and the y-component of the vector extending from the anticodon (A36) to the elbow (U56). Top right: Angle between the z-axis and the same vector as in the previous panel. These plots indicate that the tRNA flips upside down as it exits the E-site cavity, tilting preferentially toward the P-site tRNA rather than the L1 stalk. Bottom left: Angle between the x-axis and the x-component of the vector from the elbow (U56) to the 3'-CCA tail (A77). Bottom right: Angle between the z-axis and the same vector. Together, the bottom panels suggest that the 3’-CCA end rotates toward the small subunit (SSU) side, taking a route along the L1 stalk rather than toward the P-site tRNA. Similar analyses for INT3 and POST states are not shown, as they closely resemble the INT2 results. (B) Comparison of the initial tRNA conformation in the INT2 state (left) with the reoriented conformation along the dissociation pathway (right), collectively illustrating the motions described in panel A.

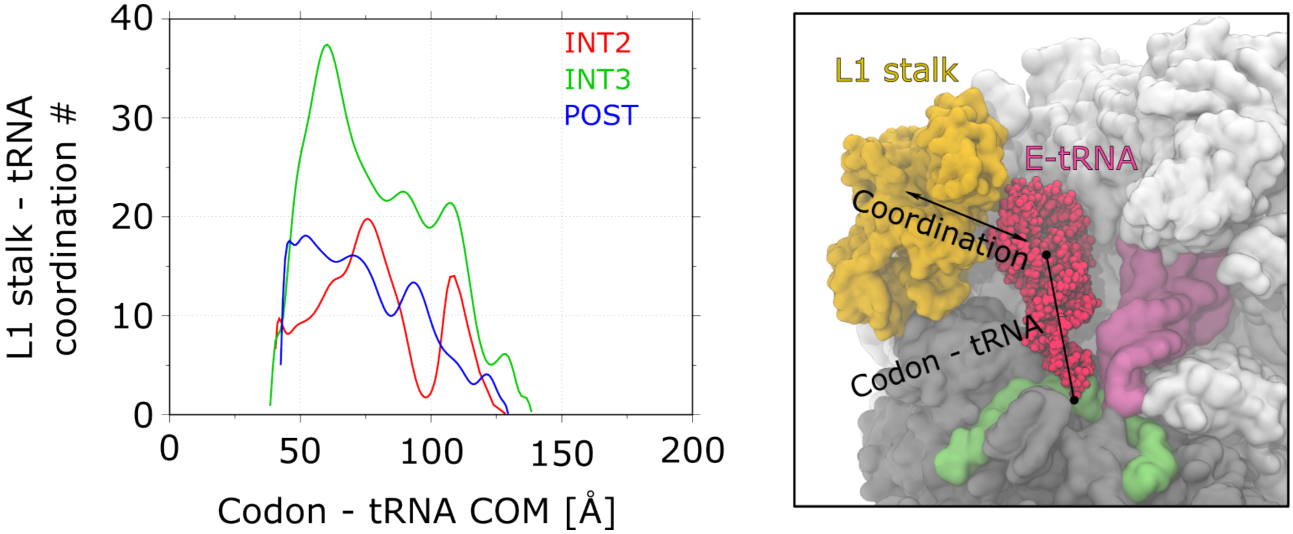

Figure S9: Coordination between the L1 stalk and tRNA across different states. Left: Coordination number between the L1 stalk and the entire tRNA plotted as a function of codon–tRNA distance for three distinct states. A pronounced twofold increase in L1–tRNA coordination is observed in the INT3 state compared to both INT2 and POST. Right: Schematic illustration of the two variables shown in the left panel.

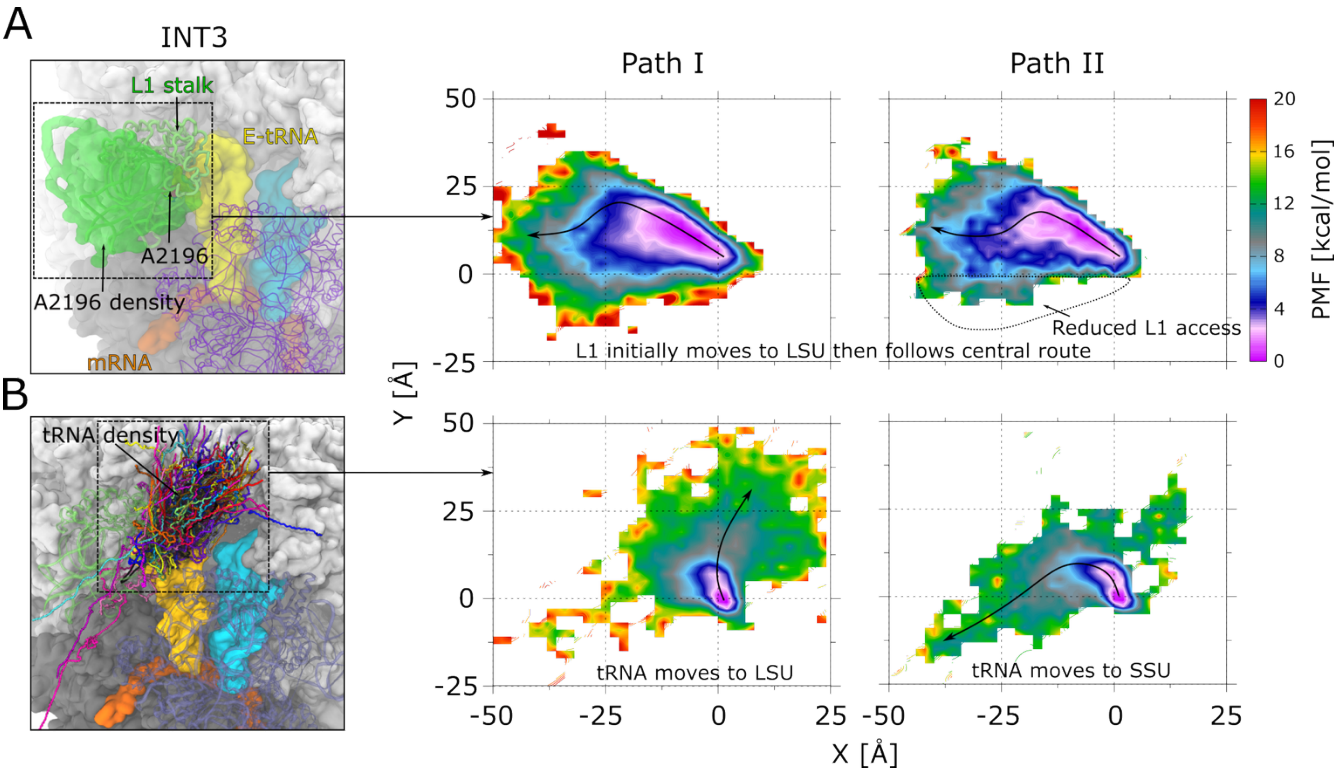

Figure S10: Coupling between L1 stalk dynamics and tRNA dissociation pathways. (A) Distribution of the L1 stalk residue A2169 during MUON simulations of the INT3 state. The distribution was separated into two sets corresponding to dissociation pathways I and II (as defined in Fig. 4A of the main text). These were projected onto the xy-plane, yielding potential of mean force (PMF) surfaces with respect to the x- and y-axes, shown in the two plots on the right. (B) Distribution of tRNA conformations from the INT3 state, similarly, divided according to pathways I and II, and used to construct two PMF landscapes. The results reveal that tRNA follows two distinct pathways, with corresponding differences in L1 stalk dynamics, as shown in panel A. Notably, during dissociation along path II, the tRNA occupies the region between the L1 stalk and the small subunit (SSU) head, thereby blocking L1 stalk access to that space. Arrows in each panel indicate the preferred direction of motion for the L1 stalk or tRNA.

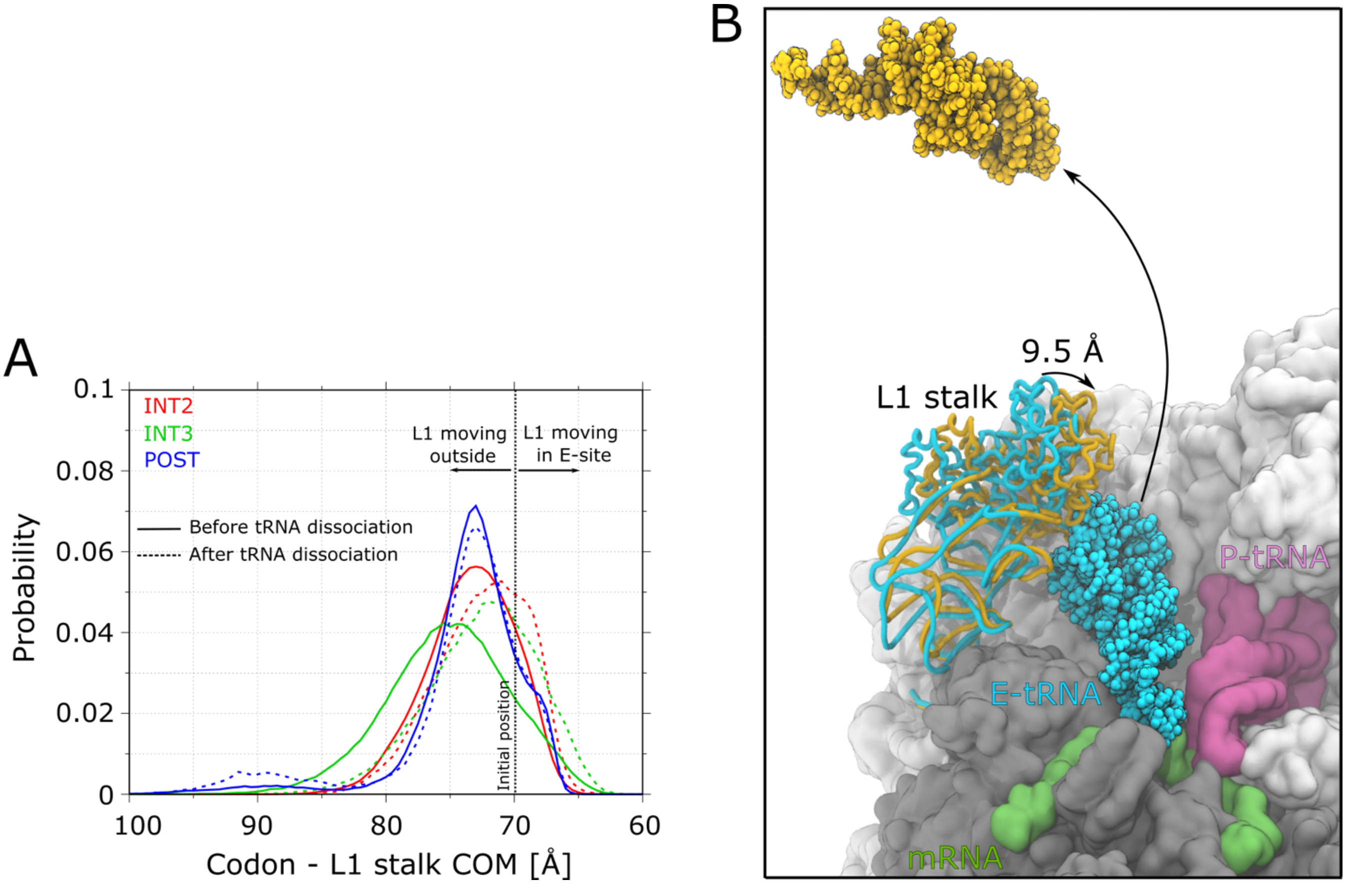

Figure S11: L1 stalk motion before and after tRNA dissociation. (A) Probability distributions of the L1 stalk distance from the E-site codon, derived from MUON trajectories. For each of the three states, distributions are shown before (solid lines) and after (dotted lines) complete tRNA dissociation. The initial position of the L1 stalk (70 Å) is marked with a vertical dashed line. (B) Representative snapshot comparing the L1 stalk position before (cyan) and after (orange) tRNA ejection, showing a displacement of ~9.5 Å within the E-site cavity following tRNA departure.

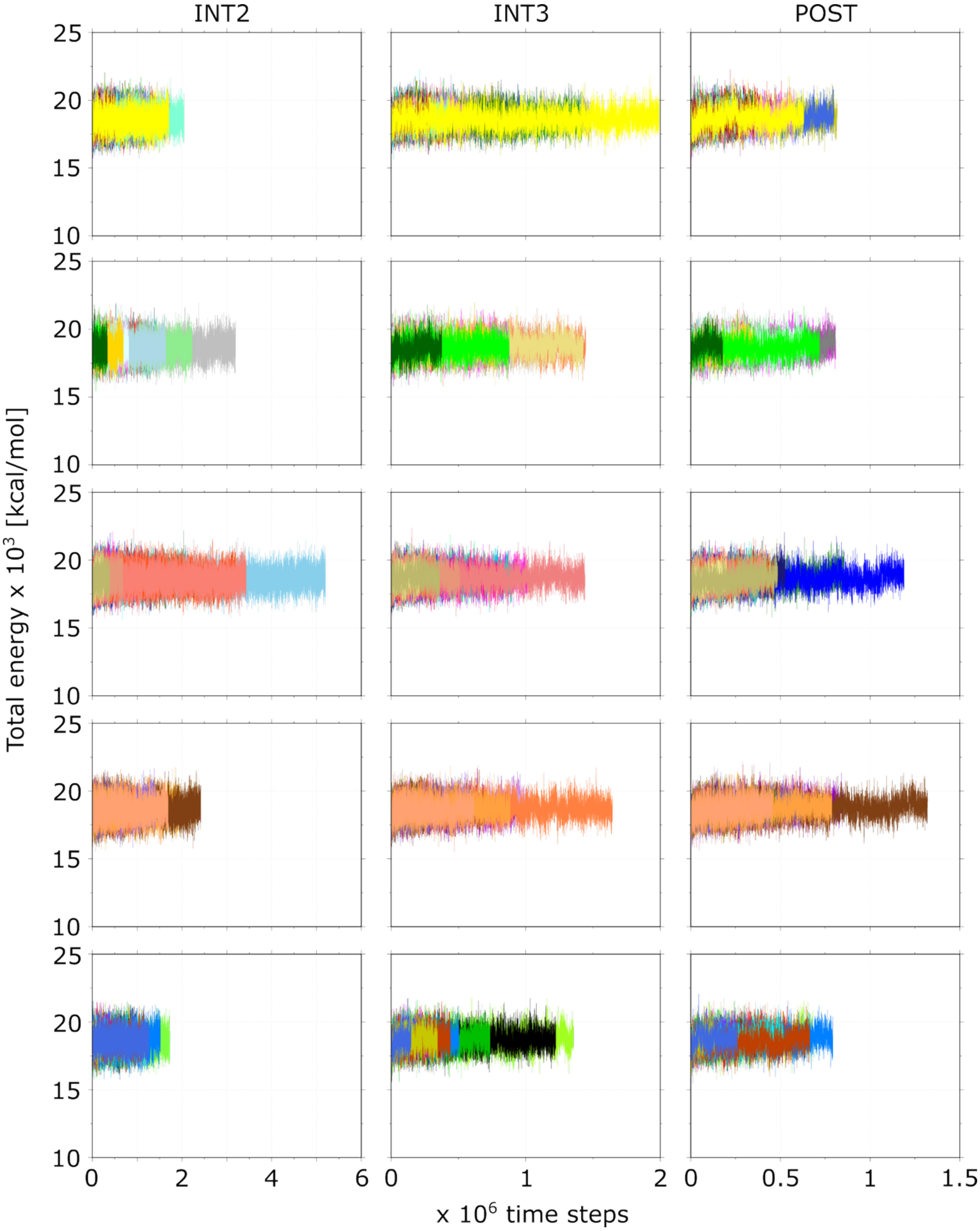

Figure S12: Conservation of total energy. For three simulated systems of ribosomes, total energy with respect to simulation time is shown for all 100 MUON trajectories across five panels (each panel showing 20 trajectories).

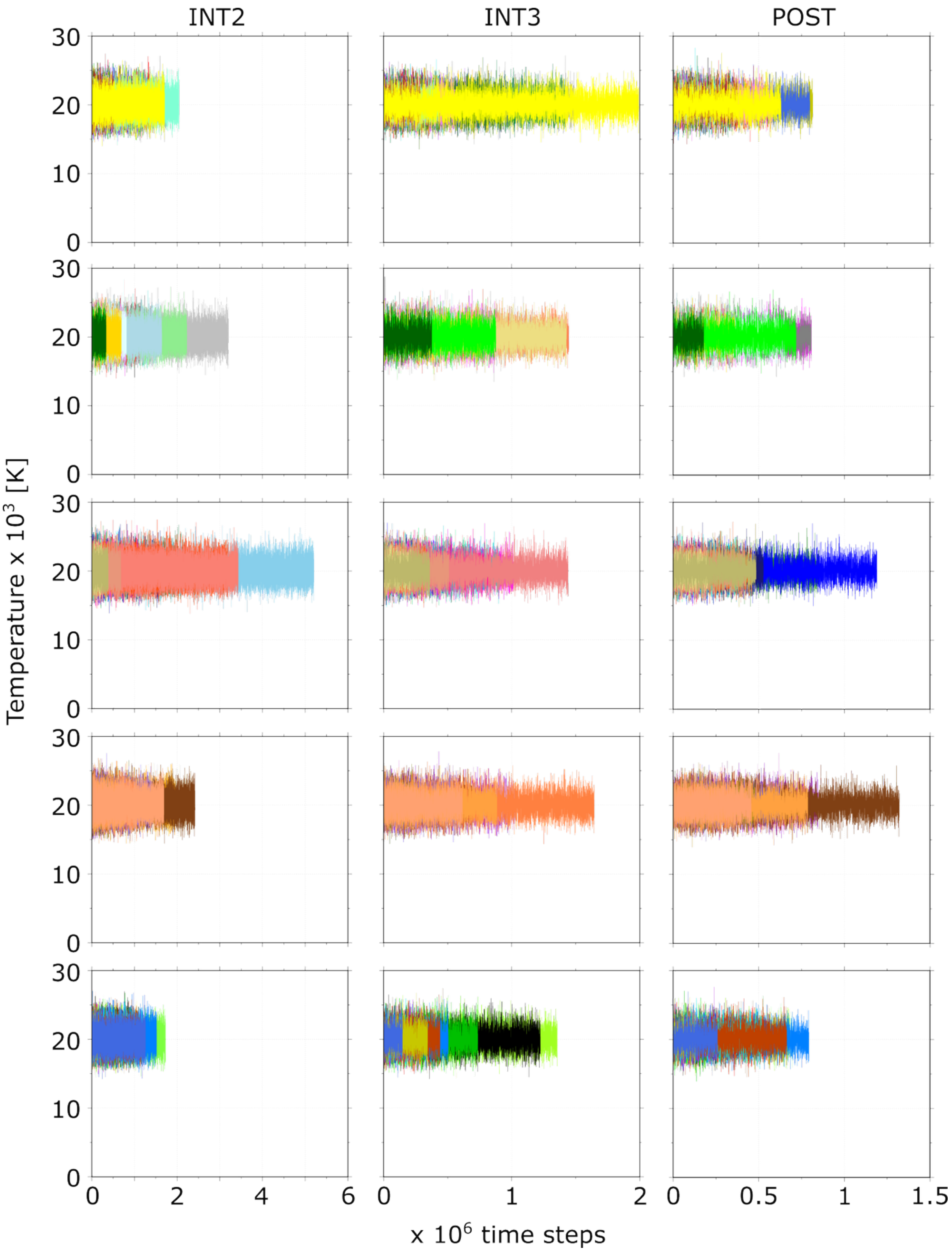

Figure S13: For three simulated systems of ribosomes, the elevated temperature with respect to simulation time is shown for all 100 MUON trajectories across five panels (each panel showing 20 trajectories).

References

1. Fei, J., Kosuri, P., MacDougall, D. D. & Gonzalez, R. L. Coupling of ribosomal L1 stalk and tRNA dynamics during translation elongation. *Mol Cell* **30**, 348–359 (2008).
2. Choi, J. & Puglisi, J. D. Three tRNAs on the ribosome slow translation elongation. *Proceedings of the National Academy of Sciences* **114**, 13691–13696 (2017).
3. Sanbonmatsu, K. Supercomputing in the biological sciences: Toward Zettascale and Yottascale simulations. *Curr. Opin. Struct. Biol.*, **88**, 102889 (2024).
4. Dama, J. F., Parrinello, M. & Voth, G. A. Well-tempered metadynamics converges asymptotically. *Phys Rev Lett* **112**, 240602 (2014).
5. Barducci, A., Bussi, G. & Parrinello, M. Well-tempered metadynamics: a smoothly converging and tunable free-energy method. *Phys Rev Lett* **100**, 020603 (2008).
6. Raiteri, P., Laio, A., Gervasio, F. L., Micheletti, C. & Parrinello, M. Efficient reconstruction of complex free energy landscapes by multiple walkers metadynamics. *J Phys Chem B* **110**, 3533–3539 (2006).
7. Tiwary, P. & Parrinello, M. A time-independent free energy estimator for metadynamics. *J Phys Chem B* **119**, 736–742 (2015).
8. Prajapati, J. D., Fernández Solano, C. J., Winterhalter, M. & Kleinekathöfer, U. Characterization of ciprofloxacin permeation pathways across the porin OmpC using metadynamics and a string method. *J Chem Theory Comput* **13**, 4553–4566 (2017).
9. Gumbart, J. C., Roux, B. & Chipot, C. Efficient determination of protein–protein standard binding free energies from first principles. *J Chem Theory Comput* **9**, 3789–3798 (2013).
10. Ovchinnikov, V., Karplus, M. & Vanden-Eijnden, E. Free energy of conformational transition paths in biomolecules: The string method and its application to myosin VI. *J Chem Phys* **134**, (2011).
11. Mills, M. & Andricioaei, I. An experimentally guided umbrella sampling protocol for biomolecules. *J Chem Phys* **129**, (2008).
12. Rodriguez, R. A., Chen, L. Y., Plascencia-Villa, G. & Perry, G. Elongation affinity, activation barrier, and stability of Aβ42 oligomers/fibrils in physiological saline. *Biochem Biophys Res Commun* **487**, 444–449 (2017).
13. Mykuliak, V. V. *et al.* Mechanical unfolding of proteins—a comparative nonequilibrium molecular dynamics study. *Biophys J* **119**, 939–949 (2020).
14. Lee, H. Effects of nanoparticle electrostatics and protein–protein interactions on corona formation: conformation and hydrodynamics. *Small* **16**, (2020).
15. Kalyaanamoorthy, S. *et al.* A structure-based computational workflow to predict liability and binding modes of small molecules to hERG. *Sci Rep* **10**, 16262 (2020).
16. Li, Y. *et al.* A wrinkled nanosurface causes accelerated protein unfolding revealing its critical role in nanotoxicity. *RSC Adv* **12**, 30976–30984 (2022).
17. Her Choong, F. & Keat Yap, B. Cell-penetrating peptides: correlation between peptide-lipid interaction and penetration efficiency. *ChemPhysChem* **22**, 493–498 (2021).
18. Preiner, J. *et al.* Free energy of membrane protein unfolding derived from single-molecule force measurements. *Biophys J* **93**, 930–937 (2007).
19. Jackola, D. R., Blackburn, C., Sveum, M. & Rosenberg, A. Entropy-favored human antibody binding reactions with a non-infectious antigen. *Mol Immunol* **45**, 1494–1500 (2008).

20. Schwesinger, F. *et al.* Unbinding forces of single antibody-antigen complexes correlate with their thermal dissociation rates. *Proceedings of the National Academy of Sciences* **97**, 9972–9977 (2000).
21. Limongelli, V., Bonomi, M. & Parrinello, M. Funnel metadynamics as accurate binding free-energy method. *Proc Natl Acad Sci U S A* **110**, (2013).
22. Sousa, C. F., Becker, R. A., Lehr, C.-M., Kalinina, O. V. & Hub, J. S. Simulated tempering-enhanced umbrella sampling improves convergence of free energy calculations of drug membrane permeation. *J Chem Theory Comput* **19**, 1898–1907 (2023).
23. Aydin, F. *et al.* Improving the accuracy and convergence of drug permeation simulations via machine-learned collective variables. *J Chem Phys* **155**, (2021).
24. Domański, J., Hedger, G., Best, R. B., Stansfeld, P. J. & Sansom, M. S. P. Convergence and sampling in determining free energy landscapes for membrane protein association. *J Phys Chem B* **121**, 3364–3375 (2017).
25. Flis, J. *et al.* tRNA translocation by the eukaryotic 80S ribosome and the impact of GTP hydrolysis. *Cell Rep* **25**, 2676-2688.e7 (2018).
26. Brown, A., Baird, M. R., Yip, M. C., Murray, J. & Shao, S. Structures of translationally inactive mammalian ribosomes. *Elife* **7**, (2018).
27. Zhang, Y., Hong, S., Ruangprasert, A., Skiniotis, G. & Dunham, C. M. Alternative mode of E-Site tRNA binding in the presence of a downstream mRNA stem loop at the entrance channel. *Structure* **26**, 437-445.e3 (2018).
28. Bock, L. V *et al.* Energy barriers and driving forces in tRNA translocation through the ribosome. *Nat Struct Mol Biol* **20**, 1390–1396 (2013).